




Pulse gas-assisted multi-needle electrospinning of nanofibers

Guojie Xu¹ · Xun Chen¹ · Ziming Zhu² · Peixuan Wu¹ · Han Wang¹ · Xindu Chen¹ · Wei Gao³ · Zhen Liu⁴ 

Received: 29 July 2019 / Revised: 29 November 2019 / Accepted: 1 December 2019 / Published online: 30 December 2019
© Springer Nature Switzerland AG 2019

Abstract

Multi-needle electrospinning is an effective method to increase the productivity of nanofibers. In this paper, the number of single-needle jets was increased to further improve the production efficiency. As the traditional method for increasing the number of single-needle jets has poor controllability and persistence, we proposed a gas-assisted method to increase the yield of nanofibers. A coaxial gas auxiliary needle was designed with an intermediate shaft supplied gas and the outer shaft supplied solution. Innovatively using pulse gas to produce continuous and stable bubbles which are ruptured on the needle. The liquid film is continuously disturbed, which generates jets in the electric field, thereby increasing the number of jets of a single needle. After optimization of the single-needle gas-assisted electrospinning process, the stable spraying process of 16-pin multi-needle electrospinning has been realized. The gas-assisted electrospinning productivity was 4.7 times higher than that of without gas assistance. It provided a new idea for improving the stable production of the multi-needle electrospinning.

Keywords Gas-assisted electrospinning · Nanofibers · Productivity improvement · Multi-needle electrospinning · Multi-jet electrospinning

1 Introduction

Electrospinning is a very simple process by which polymer nanofibers can be produced using an electrostatically driven jet of polymer solution. Significant progress has been made in this process throughout the past few years, and the nanocomposite fibers have been exploited to a wide range of applications

in the fields of biomedicine, chemical separation, catalysis, energy storage, sensors, ion recovery, etc. [1–4]. The initial production method for electrospinning was single-needle spinning with low production efficiency, which was not economical for large-scale industrial production. Common electrospinning methods for the mass production of nanofibers included multi-needle electrospinning and needle-free spinning. Needle-free spinning technology made it arduous to control the position of the spray and the morphology of the fiber, which can result in non-uniformity of the nanofiber membrane [5–7]. Multi-needle electrospinning can produce better quality nanofiber membranes, but their yields were still relatively low. Therefore, it is necessary to increase the output of single-needle electrospinning through technological improvements [8–11].

In 2008, Reneker proposed to use auxiliary electrode to obtain multi-jets in electrospinning process to improve the yield of nanofibers [12]. Yamashita used multi-notch formed on the needle tips to achieve multi-jets [13]. The methods of obtaining multi-jets by modifying spinning device also included the adoption of collectors with different structures [14]. The method of modifying spinning device was not the only choice; increasing the electric field force of tips was also adopted [15].

Gas assisted multi-jets technology is a method to increase the yield of single-nozzle electrospun nanofibers. In 2007, Liu et al. [16–18] reported a technique for exciting electrospinning

Guojie Xu and Xun Chen contributed equally to this work.

✉ Xun Chen
xunchen@gdut.edu.cn

✉ Han Wang
Wanghanguo@gdut.edu.cn

Zhen Liu
zliu@frostburg.edu

¹ Guangdong Provincial Key Laboratory of Micro-Nano Manufacturing Technology and Equipment, School of Electromechanical Engineering, Guangdong University of Technology, Guangzhou 510006, China

² Foshan Lepton Precision M&C Tech Co. Ltd, Foshan 528000, China

³ Department of Chemical and Materials Engineering, The University of Auckland, PB 92019, Auckland 1142, New Zealand

⁴ Department of Physics and Engineering, Frostburg State University, Frostburg, MD 21532, USA

with bubbles, which utilized multiple jets generated during bubble popping to realize electrospinning, greatly improving the productivity. During the bubble formation process, the bubble experiences growth and rupture. When the bubble bursts in the electrospinning, due to the gas flow and the electric field force, the breaking point is formed at the thinnest part of the bubble with the maximum tension, and then the liquid film of the bubble is curled at the point of breakage and moves toward the edge of the bubble burst. Here, the curling speed of the bubble liquid film is related to the bubble radius and the film thickness, and the curling speed is an important factor that affects the regular formation of the bubble. Therefore, if the air pressure is too large, the liquid film cannot be recovered at the rupture port, and the gas will continue to be discharged, so that bubbles cannot be formed again. Therefore, continuous gas supply is difficult to control stable and regular formation and cracking of the bubble, as well as multi-spinning with gas assist is difficult to stably control [17, 19–31].

Aiming at the problem of using multi-needle electrospinning to increase the production efficiency, this paper proposes a method that uses pulse gas to continuously disturb the regular bubble collapse at the tip to maintain multiple jets and realizes gas-assisted electrospinning. The multi-jet process is stably controlled, providing a new idea for multi-needle electrospinning to further increase nanofiber production.

2 Materials and methods

2.1 Experimental setup

The schematic diagram of the experimental setup was shown in Fig. 1. The gas and the solution were output by an inner needle with d_2 in diameter and an outer needle with d_1 in diameter, respectively, and the inner tip was shorter than the outer tip by h_1 . The inner needle, the type of which include 13G (diameter at 1.9 mm), 16G (diameter at 1.2 mm), and

20G (diameter at 0.62 mm), was controlled on or off and the air pressure by the air pressure valve. The type of the outer needle used in this paper is 8G (diameter at 3.3 mm) with 20 mm needle length. As shown in Fig. 2, t_1 is the duration of ventilation, and t_2 is the length of gas interruption. The value of t_1 and t_2 could be set separately to realize the period of pulse or constant pressure gas, and the minimum on-off time is 50 ms. The high-voltage power supply was made by Tianjin Dongwen High Voltage Co. The highest voltage is 50 kV with the highest current of 2 mA.

2.2 Material

The experimental material was an aqueous polyvinyl alcohol solution (1788 model, Since Aladdin). At room temperature of 25 °C, 4 concentrations of polyvinyl alcohol (8, 10, 12 and 14%) were used.

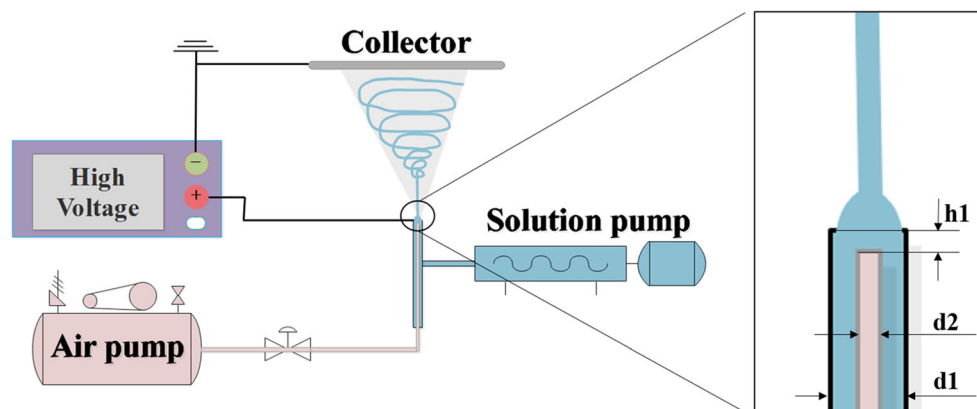
3 Theoretical analysis of gas-assisted needle electrospinning

3.1 Bubble generation theory

According to existing studies on the formation mechanism of bubbles in liquids [24, 26, 28, 32], the theoretical analysis of bubbles was carried out in this paper. In the process of forming the bubble, the height of the airhole from the liquid surface and the distance between the airhole and the diameter of the outer needle determine three states of bubble formation shown in Fig. 3: (a) the bubble connecting the airhole, (b) the bubble leaving the airhole and smaller than the diameter of the outer needle, and (c) the bubble leaving the airhole and next to the outer needle. In this paper, the experimental model was close to state (a), due to the low height of the airhole from the liquid surface.

From formation to rupture, bubbles can be divided into three stages: formation stage, expansion stage, and rupture stage. At the formation stage, shown in Fig. 6a and c, as the

Fig. 1 Schematic of the experimental setup



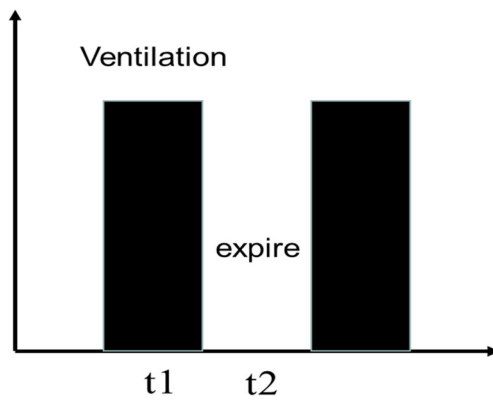


Fig. 2 Schematic of periodic pulse pressure

air is continuously injected, the convexity of the bubble tip gradually increases, and the solution thin liquid layer is lifted up to form a near spherical surface. At the same time, the thickness of the liquid layer above the bubble is continuously reduced, and the closer to the tip of the bubble, the thinner the thickness of the liquid layer. Then there is the expansion stage as shown in Fig. 7a. When the bubble volume increases gradually, the bubble shape remains spherical. And the projection of the bubble on the horizontal plane is larger than the outer needle cross section. At the final rupture stage, the bubble is gradually elongated in the longitudinal direction until cracking occurs when the thickness of the liquid film is lowered to a certain extent, as shown in Fig. 8.

3.2 Fluid dynamics theory of bubble in an electric field

3.2.1 Fluid dynamics in an electric field

There are thermally excited capillary waves, whose amplitude and wavelength are controlled by the interfacial tension and other pressures acting on the interface, on the free surface. The presence of surface tension suppresses the amplification of the capillary waves. When an electric field is applied to the

interface, electrostatic pressure can be generated at the interface. Because the direction of electrostatic pressure is the opposite of surface tension, the electrostatic pressure can overcome the surface tension when a sufficiently large voltage is applied, which causes the interface fluctuations to amplify and the liquid surface to undulate [33, 34].

The thin layer of liquid in the electric field is mainly affected by four forces: atmospheric pressure, surface tension, electrostatic pressure, and separation pressure. So the overall pressure on the liquid layer is [34]

$$p = p_o - \gamma \frac{\partial^2 h}{\partial x^2} + p_{ei}(h) + P_{dis}(h) \quad (1)$$

where p_o is atmospheric pressure; $\gamma \frac{\partial^2 h}{\partial x^2}$ represents Laplace pressure, which is caused by the change of interface energy caused by the change of interface area; p_{ei} is the electrostatic pressure, P_{dis} is the separation pressure; and h is the thickness of the liquid layer. The separation pressure is caused by the Van der Waals interaction, and its value is much smaller than the Laplace pressure, so it can be neglect in general.

In this paper, we only analyze the case where the surface disturbance wavelength λ is much larger than the liquid layer thickness variation value. In this case, the electric field force is not enough to overcome the surface pressure to form the liquid column connecting the two electrodes. The polymer thin layer fluctuation amplification diagram is shown in Fig. 4.

For two-layer media, the formula for calculating the field strength is [20].

$$E_i = \frac{\varepsilon_j U}{\varepsilon_1 h_2 + \varepsilon_2 h_1} \quad (i, j = 1, 2; i \neq j) \quad (2)$$

where 1 and 2 represent the type of media; h_1 and h_2 are thickness parameters of the media 1 and 2, respectively; and ε_1 and ε_2 refer to the dielectric constants of the media 1 and 2, respectively.

For the liquid-gas medium between the electrodes, as shown in Fig. 4, it can be seen that there are the four

Fig. 3 Three states of bubble formation

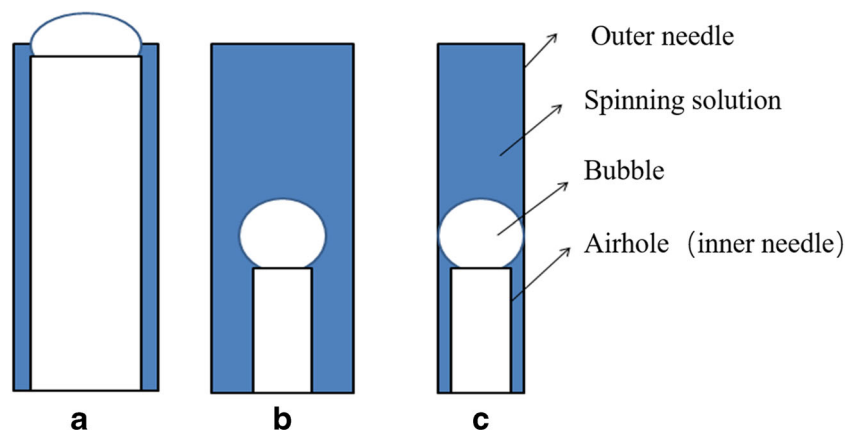
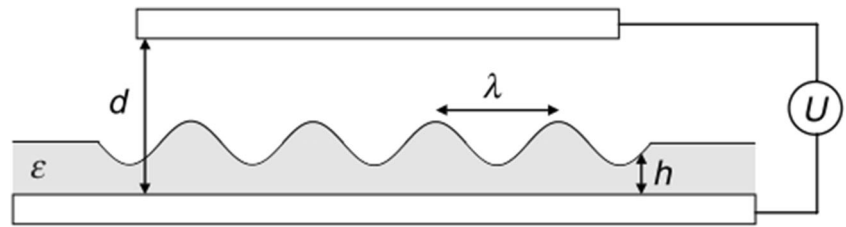


Fig. 4 Polymer thin layer surface fluctuation amplification [34]



parameters: the distance between the two electrodes d , the gas thickness between the electrodes ($d-h$), the thickness of the liquid layer h , and the supply voltage is U . So the electric field strength of the liquid layer is

$$E_p = \frac{\epsilon_r U}{\epsilon_r h + \epsilon_p (d-h)} \tag{3}$$

And the electric field strength of the gas layer is

$$E_r = \frac{\epsilon_p U}{\epsilon_r h + \epsilon_p (d-h)} \tag{4}$$

where ϵ_p is the liquid layer dielectric constant; where ϵ_p is the gas dielectric constant, $\epsilon_r \approx 1.0$. Thus the electric field strength of the liquid layer is

$$E_p = \frac{U}{\epsilon_p d - (\epsilon_p - 1)h} \tag{5}$$

and the electric field strength of the gas layer is

$$E_r = \epsilon_p E_p \tag{6}$$

In addition, the interface electrostatic pressure is calculated as [35].

$$p_{ei} = -\epsilon_0 (\epsilon_p - \epsilon_r) E_r E_p \tag{7}$$

From eqs. (6) and (7), the interface electrostatic pressure is

$$p_{ei} = -\epsilon_0 \epsilon_p (\epsilon_p - 1) E_p^2 \tag{8}$$

where ϵ_0 is the vacuum dielectric constant.

3.2.2 Calculation of surface charge density of liquid film

In the uniform electric field E_0 , the surface of the spherical bubble generates an induced charge, and the charge is distributed on the surface of the bubble due to the Coulomb force. The surface density of these induced charges is not uniform under the electric field, as well as the charge migrates to the local tip position of the bubble along the direction of the electric field force [30]. Moreover, the larger the surface curvature, the denser the charge distribution. Figure 5 shows the actual charge distribution of spherical bubbles in a uniform electric field.

In a spherical conductor with a field strength of E_0 , the field strength at any point on the surface is [36].

$$E = 3E_0 \cos\theta \tag{9}$$

where θ is the angle between the line connecting the point and the center of the circle and the direction of E_0 .

The distribution of induced charges on the surface of a spherical conductor is related to the distribution of field strength. And the relationship between charge surface density and the electric field strength is

$$E = \frac{q}{\epsilon} \tag{10}$$

where q is the charge surface density and ϵ is the dielectric constant of the space medium. From Eqs. (9) and (10), the surface density of the induced charge on the surface of the spherical conductor is [37]

$$q = \epsilon E = 3\epsilon E_0 \cos\theta. \tag{11}$$

It can be seen that the charge density at the tip of the bubble is the largest, which is

$$q_{\max} = \epsilon E = 3\epsilon E_0 \tag{12}$$

3.3 Force analysis of bubble in an electric field

In this paper, the experimental model was close to state as shown in Fig. 3a.

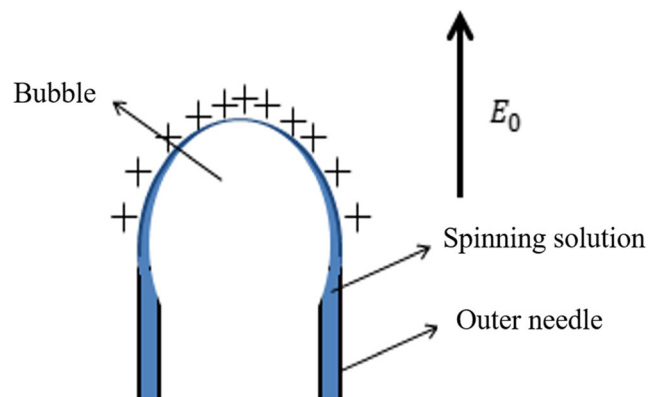


Fig. 5 The charge distribution of spherical bubble in a uniform electric field

(1) Force Analysis at the Formation Stage

As shown in Fig. 6a is a schematic diagram of the coaxial needle with the inner needle outputting air and the outer needle outputting solution. When the inner needle guarantees a certain air pressure, the solution forms a thin layer at the tip of the needle under air pressure. In the solution thin layer, shown in Fig. 6c, the bubble is mainly affected by seven kinds of forces: surface tension F_γ , electric field force F_E , static pressure F_p , gas flow momentum force F_M , inertial force F_I , viscous resistance F_D , and bubble inner pressure F_{in} .

In this paper, inertial force, viscous resistance, and bubble inner pressure were negligible because of small airflow. Since surface tension is generated on both upper and lower surfaces of the liquid layer, the surface tension on the bubble is

$$F_\gamma = 2\pi r \cdot \gamma \cos\theta + 2\pi r_0 \cdot \gamma \cos\theta \tag{13}$$

where r is the radius of the outer needle, r_0 is the radius of the inner needle, γ is the surface tension, and θ is the angle between the direction of surface tension and the vertical direction.

It is assumed that the thickness of the solution above the bubble is uniform at the formation stage. And the bubble below the liquid layer in the gravitational field is subjected to the static pressure of the fluid. According to the calculation formula of static pressure, the static pressure of the bubble is

$$F_p = \pi r_0^2 \cdot (\rho g z + p_0) \tag{14}$$

where ρ is the liquid density, z is the thickness of the solution layer, and p_0 is the atmospheric pressure.

Due to the presence of air pressure, the bubble is subjected to force from the inside to the outside. The horizontal projection of the bubble just coincides with the inner needle outlet, so the vertical upward force caused by the pressure inside the bubble is

$$F_{in} = p \cdot \pi r_0^2 \tag{15}$$

where p is the internal pressure of the bubble.

According to the previous analysis from Eqs. (5) and (8), the electrostatic pressure of the bubble is

$$p_{el} = \epsilon_0 \epsilon_P (\epsilon_P - 1) \cdot \left[\frac{U}{\epsilon_P d - (\epsilon_P - 1)z} \right]^2 \tag{16}$$

where d is the distance from the collector to the needle tip and z is the thickness of the liquid layer above the bubble.

Thus, the electric field force of the bubble in the vertical direction is

$$F_E = p_{el} \cdot \pi r_0^2 \tag{17}$$

From the force analysis as shown in Fig. 6c, the relationship of forces can be expressed as follows:

$$F_M + F_{in} + F_E \geq F_\gamma + F_p + F_I + F_D \tag{18}$$

Since the air flow is small in this experiment, the inertial force, gas flow momentum force, and the viscous resistance were negligible. Thus,

$$F_{in} \geq F_\gamma + F_p - F_E \tag{19}$$

The required internal air pressure of the bubble is

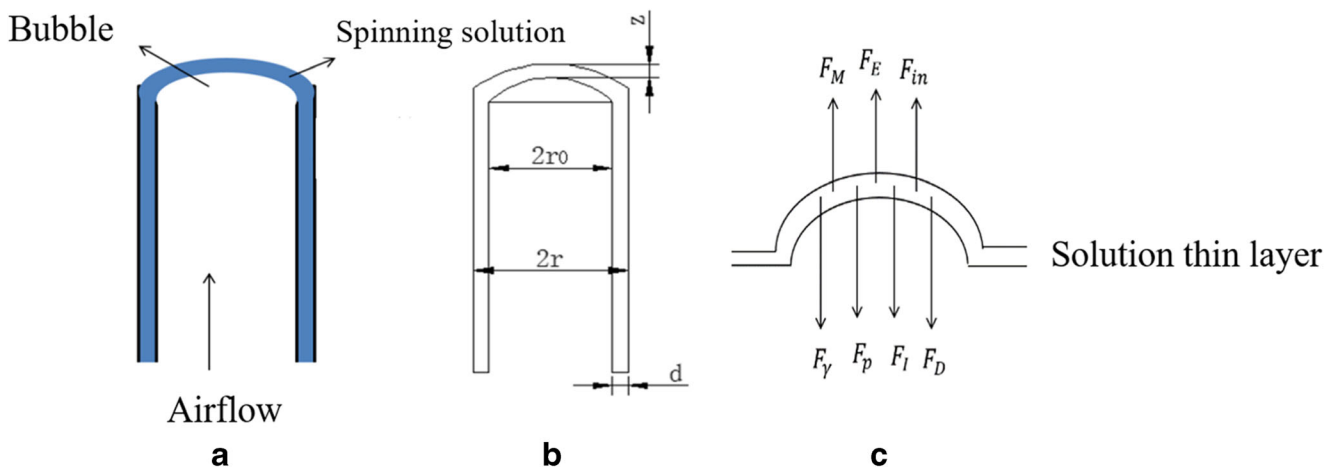


Fig. 6 Schematic diagram of bubble forming period: (a) schematic diagram of needle; (b) schematic diagram of parameters; (c) force of solution thin layer

$$p \geq \frac{1}{\pi r_0^2} \left\{ 2\pi r_0 \gamma \cos\theta + 2\pi r_0 \gamma \cos\theta + \pi r_0^2 \cdot (\rho g z + p_0) - \varepsilon_0 \varepsilon_P (\varepsilon_P - 1) \cdot \left[\frac{U}{\varepsilon_P d - (\varepsilon_P - 1) z} \right]^2 \cdot \pi r_0^2 \right\} \tag{20}$$

(2) Force Analysis at the Expansion Stage

At this stage, as the bubble volume increases, the bubble radius R increases to be larger than the radius of the inner needle, as shown in Fig. 7b. Figure 7c shows that the bubble is subjected by seven forces: surface tension F_γ , atmospheric pressure F_0 , gas flow momentum force F_M , inertial force F_I , bubble inner pressure F_{in} , viscous resistance F_D , and electric field force F_E .

Since the bubble is in the air at this time, it contains inner and outer liquid films, and the two liquid films generate additional surface force due to the surface tension. So

$$F_\gamma = 4\pi r_0 \gamma \cos\theta \tag{21}$$

And the atmospheric pressure of the bubble is

$$F_0 = \pi R^2 p_0 \tag{22}$$

The upward force caused by the internal pressure of the bubble is

$$F_{in} = p \cdot \pi R^2 \tag{23}$$

As shown in Fig. 7c, since the bubble is below the liquid film rather than the liquid layer, this case is not in the scope of electrohydrodynamic analysis. According to the previous analysis, the distribution of induced charges on the surface of the bubble is not uniform, and there is a maximum charge

density at the tip. The bubble is subjected to an electric field force in the electric field opposite to the direction of the surface tension, and the electric field force at the tip is the largest.

Because the thickness of the liquid film is almost negligible, the medium between the electrodes can be regarded as air only, and the dielectric constant of the air is $\varepsilon_r \approx 1.0$. According to the above analysis, the maximum electric field force of the bubble at the tip is

$$F_{E,max} = q_{max} E = 3\varepsilon_r E_0 \cdot 3E_0 = 9E_0^2 \tag{24}$$

And the electric field strength E_0 is

$$E_0 = \frac{U}{D} \tag{25}$$

where U is the supply voltage, D is the distance from the collector to the electrode, and q is the surface charge density of the bubble.

As the expansion process progresses, the bubble eventually ruptures at the point where the force is strongest. The critical point at which the bubble bursts depends on the force at the tip, so in order to determine the critical point of bubble burst, we can assume that each point on the bubble is subjected to the maximum electric field force. Then the total electric field force that the bubble is subjected to be expressed as $\varepsilon\varepsilon\varepsilon$

$$F_E = F_{E,max} \cdot \pi R^2 = 9E_0^2 \pi R^2 = \frac{9U^2 \pi R^2}{D^2} \tag{26}$$

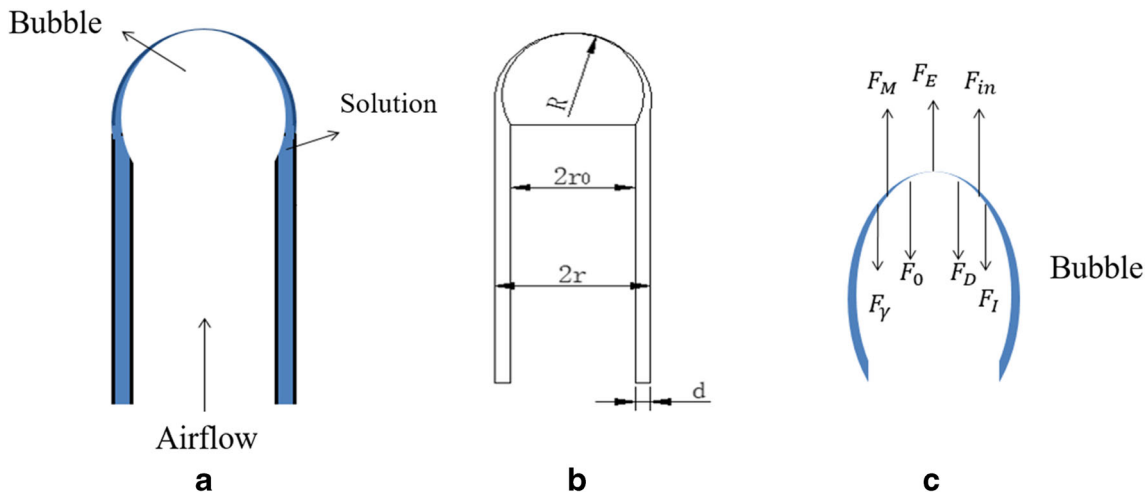
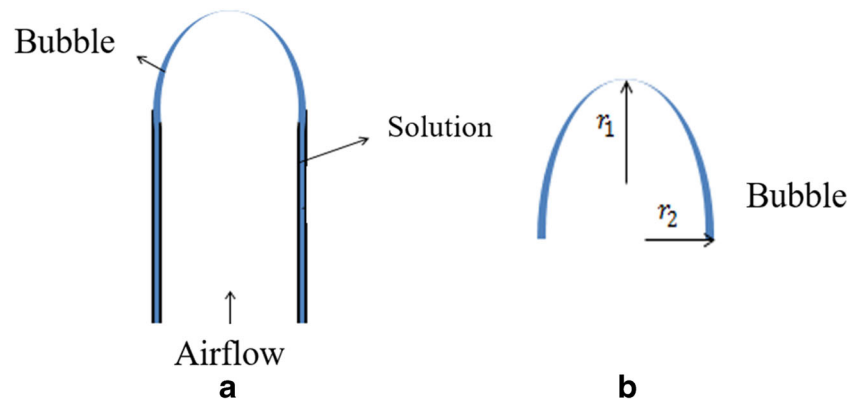


Fig. 7 Schematic diagram of bubble expansion period: (a) schematic diagram of needle; (b) schematic diagram of parameters; (c) force diagram of the bubble in the electric field

Fig. 8 Schematic diagram of bubble rupture period: (a) schematic diagram of needle; (b) schematic diagram of the radius of curvature of the bubble



From the force analysis as shown in Fig. 7c, the relationship of forces can be expressed as follows:

$$F_M + F_{in} + F_E \geq F_\gamma + F_0 + F_I + F_D \quad (27)$$

Since the air flow is small in this experiment, the inertial force, the gas flow momentum force, and the viscous resistance were negligible. Therefore

$$F_{in} \geq F_\gamma + F_0 - F_E \quad (28)$$

So the required internal air pressure of the bubble is

$$p \geq \frac{1}{\pi R^2} (4\pi r_0 \cdot \gamma \cos\theta) + p_0 - \frac{9U^2}{D^2} \quad (29)$$

(3) Force Analysis at the Rupture Stage

At this stage, the bubble no longer maintains a spherical surface, which begins to be stretched and develops toward the ellipsoid, and the bubble quickly ruptures at the tip. The bubble before rupture is also subject to seven forces: surface

tension, atmospheric pressure, gas flow momentum force, inertial force, viscous resistance, bubble inner pressure, and electric field force. At this time, the force analysis of the bubble is as shown in Fig. 7c too.

As shown in Fig. 8b, the curved surface of the bubble is determined by two radius of curvature r_1 and r_2 , and the surface force formed by the surface tension should be

$$F_\gamma = 2\gamma \left(\frac{1}{r_1} + \frac{1}{r_2} \right) \cos\theta \cdot \pi r_0^2 \quad (30)$$

The atmospheric pressure of the bubble is

$$F_0 = \pi r_2^2 \cdot p_0 \quad (31)$$

And the bubble inner pressure is

$$F_{in} = \pi r_2^2 \cdot p \quad (32)$$

The expression of the electric field force is the similar to the previous stage:

$$F_E = \frac{9U^2 \pi r_2^2}{D^2} \quad (33)$$

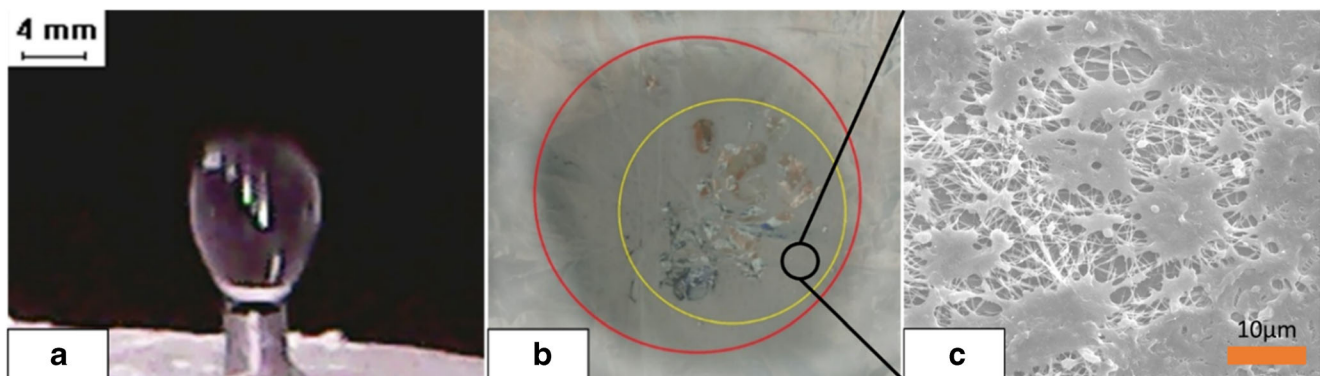
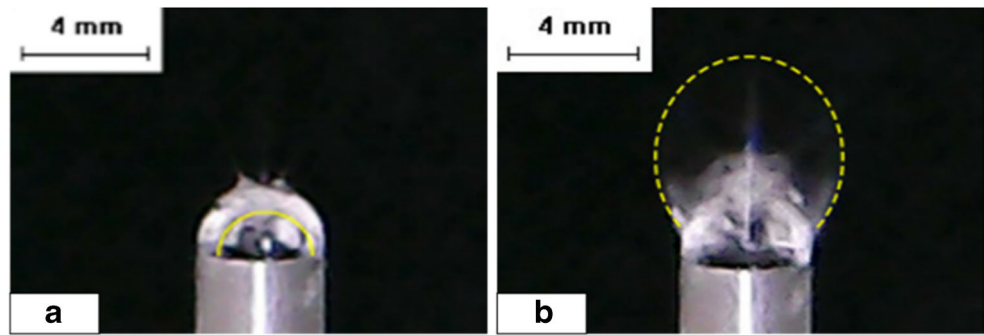


Fig. 9 (a) Bubble morphology in an electric field at constant air pressure, (b) spinning deposition at constant air pressure; (c) SEM image of the yellow circle

Fig. 10 Pulse bubble morphology: (a) the appearance of the bubble before the rupture; (b) the moment of bubble rupture



Due to

$$F_{in} \geq F_{\gamma} + F_0 - F_E \tag{34}$$

the required internal air pressure of the bubble is

$$p \geq \frac{1}{\pi r_2^2} \left[2\gamma \left(\frac{1}{r_1} + \frac{1}{r_2} \right) \cos\theta \cdot \pi r_0^2 \right] + p_0 - \frac{9U^2}{D^2} \tag{35}$$

3.4 Calculation of air pressure pulse period

From the bubble formation to the complete disappearance process, the bubble experienced two periods of growth and rupture. In the growth period, the bubble volume becomes larger and larger, and accordingly, it is necessary to maintain a certain gas flow rate. And the growth time is recorded as t_g . In gas-assisted electrospinning, during the bubble rupture period, the bubble breaks and is stretched into a nanofiber in the electric field. At this time, it is only necessary to maintain the gas pressure so that the spinning solution does not enter the gas needle until the liquid layer re-covers the tip of the inner needle. The time required to rupture to disappear is recorded as t_b . Thus, the airflow pulse period is

$$t = t_g + t_b \tag{36}$$

At the critical state of growth and rupture, the two radius of curvature of the bubble are r_1 and r_2 . It can be approximated as

follows: $r_2 \approx r$, where r is the radius of the outer needle. When the gas flow rate is very low, the bubble is always in the sub-equilibrium state [38], which can be regarded as the force balance during the critical rupture of the bubble. So r_1 is

$$r_1 = \frac{2\gamma\pi r_0^2 r \cos\theta}{\left(p - p_0 + \frac{9U^2}{d^2} \right) \pi r^3 - 2\gamma\pi r_0^2 \cos\theta} \tag{37}$$

from Eq. (35). It can be seen that the hemisphere volume at the critical rupture of the bubble is

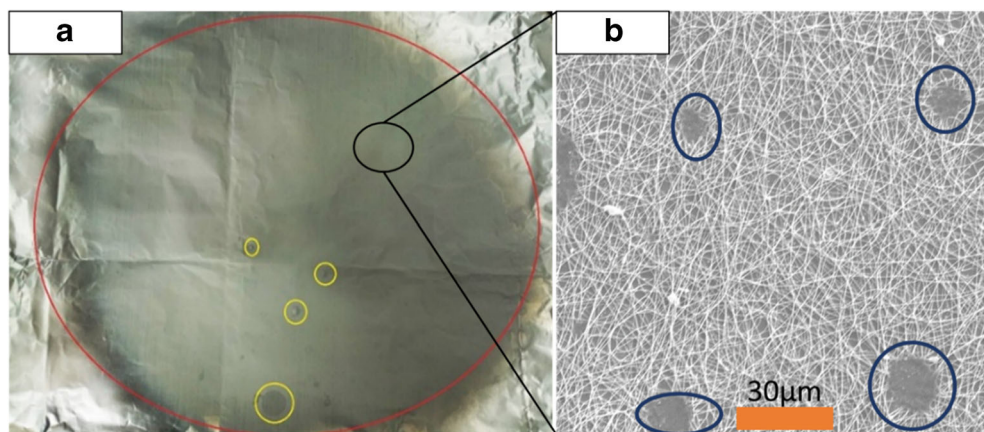
$$V_g = \frac{1}{2} \cdot \frac{4}{3} \pi r_1 r_2^2 = \frac{2}{3} \pi r_1 r^2 \tag{38}$$

Assuming the inner needle gas flow rate is Q , t_g is

$$t_g = \frac{Q}{V_g} \tag{39}$$

When the bubble breaks in the electrospinning, a crack point is generated at the thinnest portion of the bubble due to the effect of the air flow and the electric field force, and then the liquid film is curled at the break point to form a ring to move toward the edge. When the electric field force and the centripetal force of the ring are greater than the surface tension, the force system is no longer balanced. The ring breaks to produce droplets, which are stretched into nanofiber in the electric field.

Fig. 11 Spinning reception under pulsed air pressure (45kv, 12 wt% PVA aqueous solution)



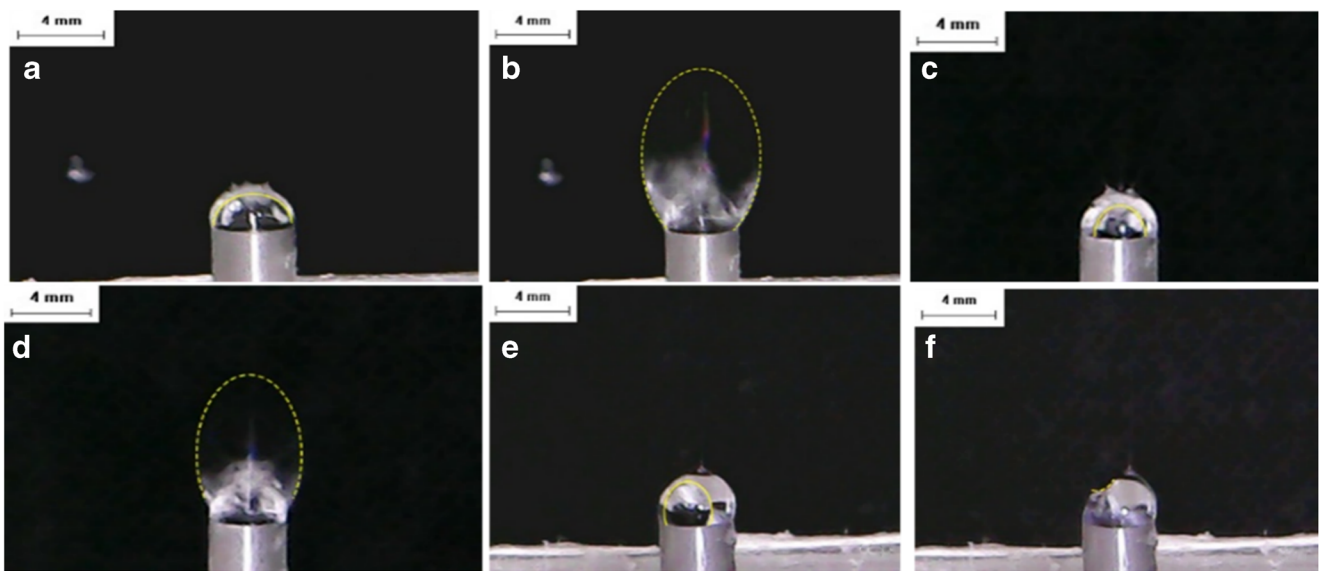


Fig. 12 Bubble morphology of different types of needle: (a), (c), and (e) using 8G–13G, 8G–16G, and 8G–20G needles before bubble rupture; (b), (d), and (f), using 8G–13G, 8G–16G, and 8G–20G needles the instant of bubble rupture (45 kV, 10 wt.% PVA solution, $t_1 = 100$ ms, $t_2 = 2000$ ms)

Although the curling speed of the bubble liquid film is related to the bubble radius and the film thickness, the liquid film curling speed fluctuation due to the uneven film thickness is not large, according to the experience of the researchers.

Therefore, the liquid film thickness can be assumed to be uniform when calculating [38].

There is an empirical formula between the curling speed u of the liquid film and the radius of curvature R of the bubble [31, 39]:

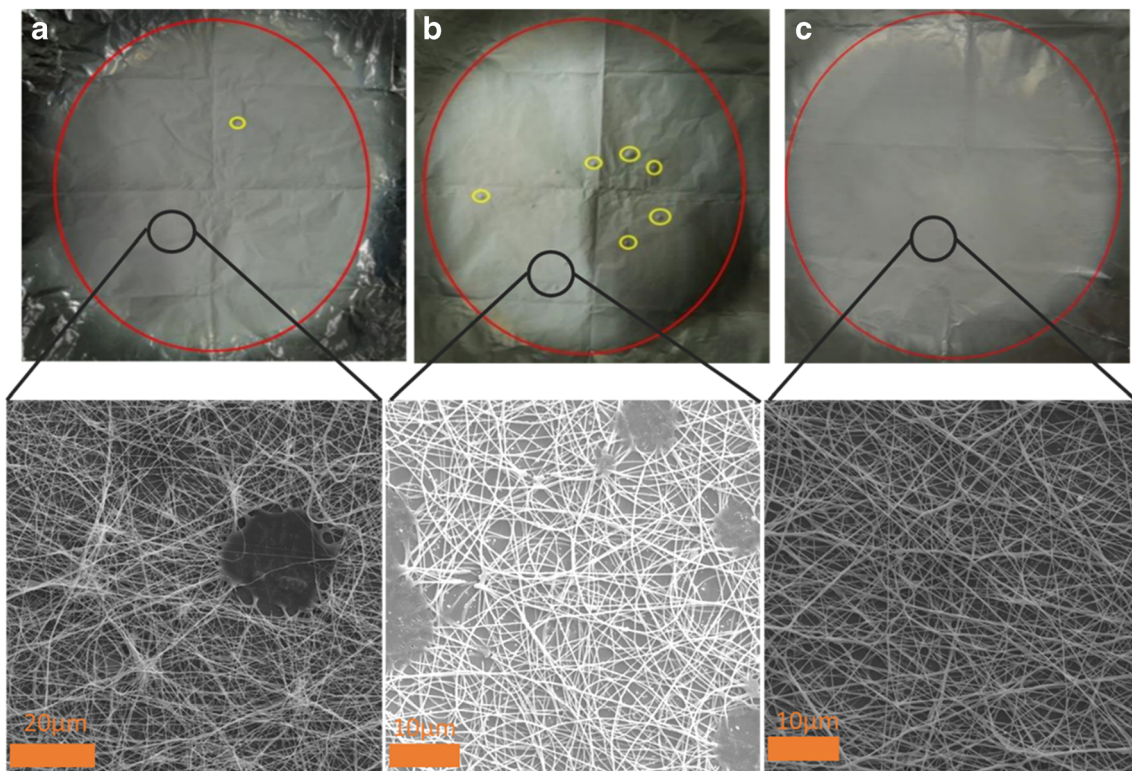
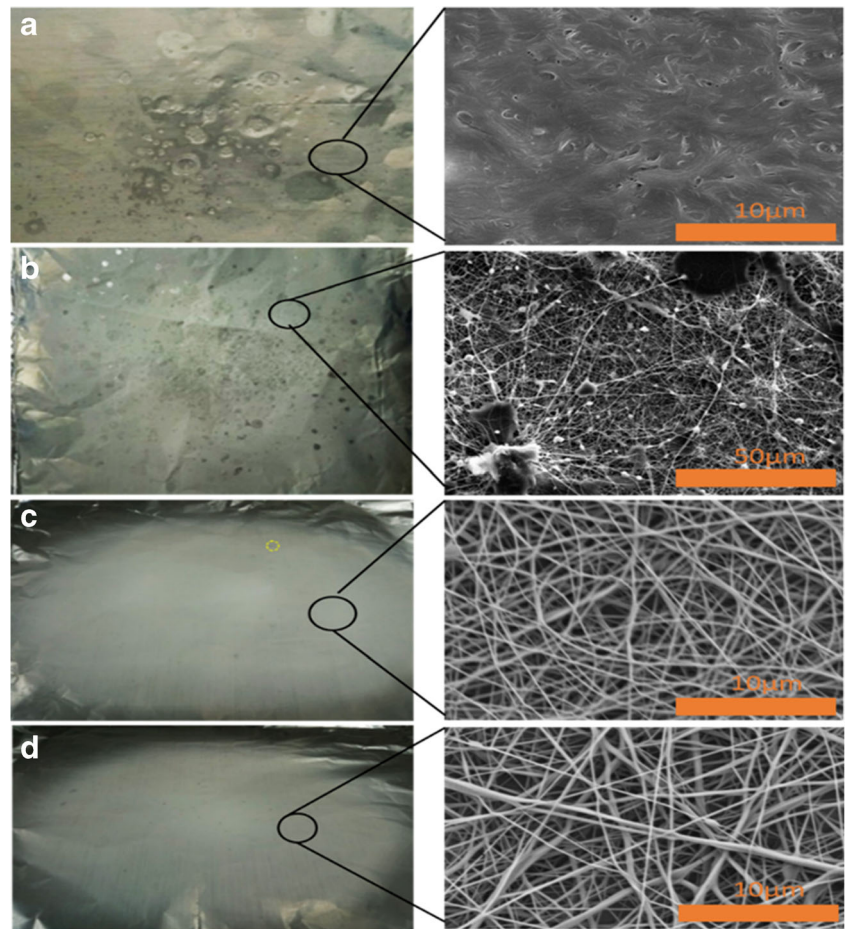


Fig. 13 After half an hour of different needle spinning: (a) 8G–13G needle; (b) 8G–16G needle; (c) 8G–20G needle. (45 kV, 12 wt.% PVA solution, $t_1 = 100$ ms, $t_2 = 2000$ ms)

Fig. 14 Spinning of different concentrations of spinning solution: (a) 8 wt% PVA; (b) 10 wt% PVA; (c) 12 wt% PVA; (d) 14 wt% PVA (8G–13G needle, $t1 = 100$ ms, $t2 = 2000$ ms, 45 kV)



$$u = aR^{-b} \tag{39}$$

where a and b are empirical coefficients.

The bubble can be regarded as an ellipse as shown in Fig. 8b, and the ellipse circumference is

$$L = 2\pi r_2 + 4(r_1 - r_2) \tag{40}$$

In order to ensure that the liquid film can completely disappear, when calculating the liquid film curling speed, we take the larger radius of curvature r_2 to calculate, and then the time from the crack to the disappearance of the liquid film is

$$t_b = \frac{L/4}{u} = \frac{\pi r_2 + 2(r_1 - r)}{2ar_2^{-b}} = \frac{\pi r_2 + 2(r_1 - r)}{2ar^{-b}} \tag{41}$$

In summary, if the air pressure is too large, the liquid film cannot be re-covered after the rupture period. The gas continues to be output, and the bubbles cannot be formed twice. Therefore, pulsed airflow was used to control the formation of bubble regularly in this paper.

4 Experimental results and discussion

4.1 Effect of air pressure time period on bubble forming and spinning

In this section, 8G needle was used for the liquid supply of outer layer, and 16G needle was used for the inner layer to supply air. The spinning solution was 12% PVA with 20 cm spinning distance and 45 kV voltage. The constant air pressure of 0.9 kPa and pulse pressure of 10 kPa ($t1 = 100$ ms, $t2 = 1000$ ms) were applied.

Figure 9 showed the bubble morphology and fiber disposition on the receiving aluminum foil. The bubble diameter was larger than the diameter of the inner needle. At this time, the film of the bubble was very thin, and the size of the bubble could not easily be controlled. The bubble was easily detached from the needle tube before its rupture. After the bubble left the needle, it was easy to directly hit the collector, causing a large piece of liquid film which did not stretch into a filament in the deposited fiber, as shown in the area inside the yellow circle of Fig. 9b. Therefore, the constant air pressure produces poor quality fibers.

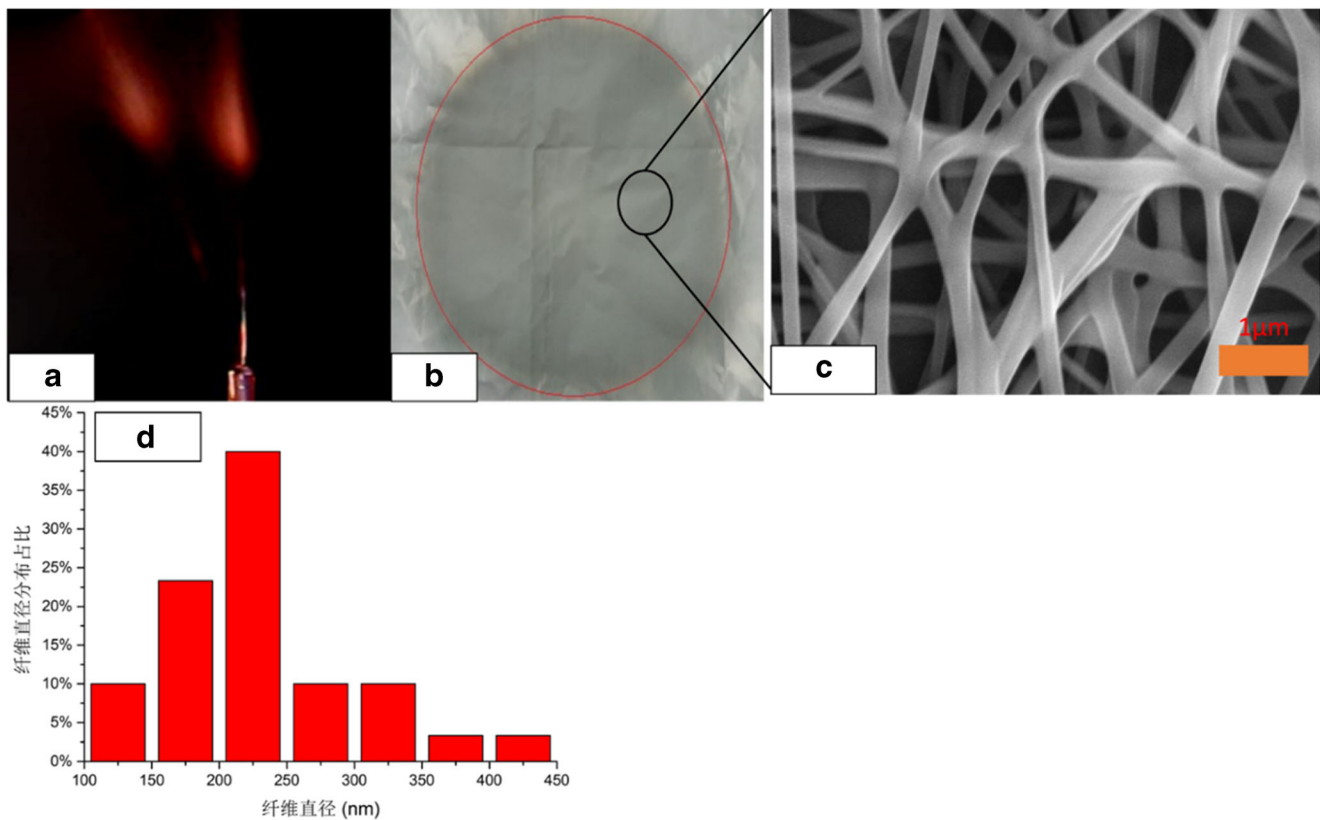


Fig. 15 (a) Jet morphology produced by a conventional 8G needle at 45 kV; (b) ordinary single 8G needle fiber morphology; (c) the SEM image of the sample; (d) the statistical distribution of the SEM nanofiber diameter of the sample

When the needle tube supplied constant air pressure and the pressure is high, the solution cannot cover the air tube mouth after the bubble burst, so the next bubble was not inducible. At this time, if the pulse gas pressure is applied, the solution would have enough time to cover the needle during the gas shut-off period, and when the next pulse gas comes, there would be enough air pressure to break through the liquid film to form a continuous liquid disturbance. During the pulse ventilation, the gas pressure and the flow force are large, and the solution layer instantaneously breaks, so the bubble has no time to grow. The bubble morphology is shown in Fig. 10.

When a voltage is applied to a bubble, the bubble subjects to an upward electric field force, so the size of the bubble increases, and the bubble formed by the moment when the solution layer breaks and also is elongated. Compared with the constant air pressure, when the pulse gas is used, the bubble has a smaller size than the needle tube due to the air pressure in the tube during the gas-off period. Figure 10a shows the bubble is in the yellow circle area. Figure 10b shows that the gas is rushing out at the moment of venting, the bubble instantly becomes large and ruptures at the needle, and the edge of the ruptured liquid film rapidly induced multiple jets.

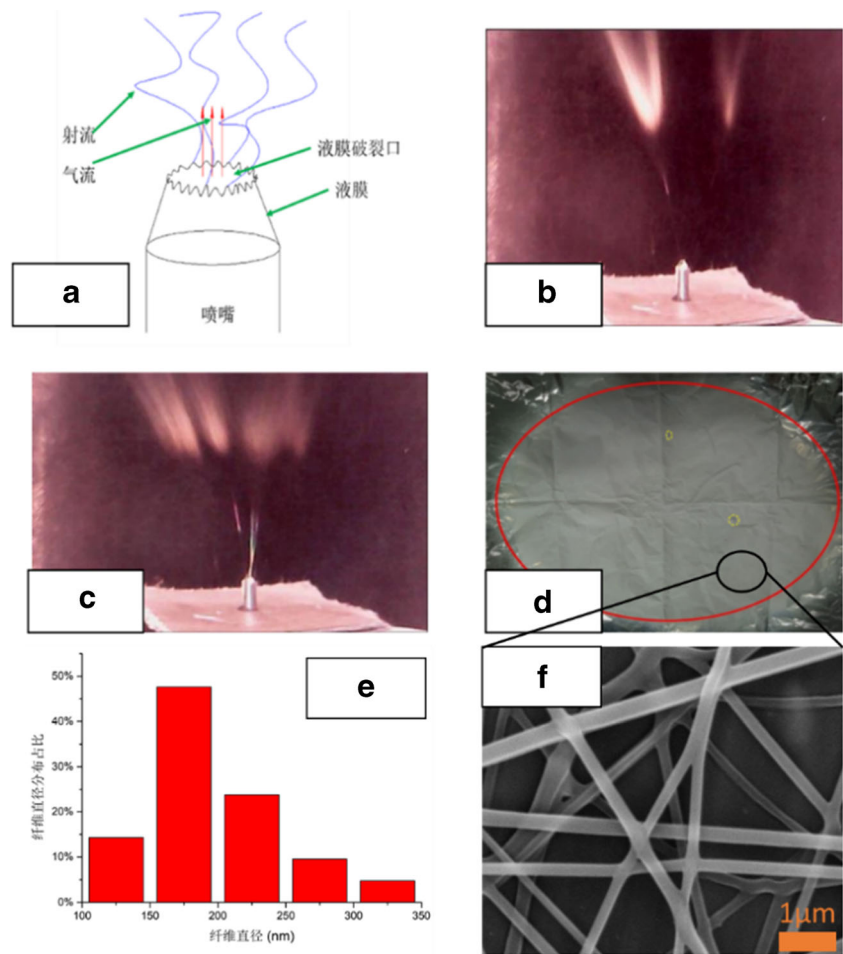
Compared with using constant air pressure, the pulse gas does not cause large air bubbles to deposit onto the collector, and the spinning process can keep stable for a long time.

Experiments showed that when using single needle with a pulse gas pressure under 0.1 MPa, $t_1 = 100$ ms and $t_2 = 1500$ ms, the bubbles generated were relatively stable and suitable for continuous spinning. However, as the spinning progressed, occasionally there would be small bubbles on the collector, as shown in yellow circles in Fig. 11. This was because the liquid film did not stretch into fiber in the air and directly flew to the collector.

4.2 Effect of needle diameter on spinning process

The gas pressure of bubble liquid film is related to the diameter of gas supply needle, while the size of bubble is affected by the spinning voltage and spinning stability. Figure 12 a–d show when the 8G–13G needle and 8G–16G needle were used for spinning, the bubble morphology and cracking process were similar, while the bubble size generated by the 8G–13G needle was larger than that of 8G–16G needle. When the 8G–20G needle was used, as the inner diameter of gas needle was small, the size of bubble was small and wrapped by thick solution. At the moment of ventilation, the solution was pushed out from a small hole (yellow dot line in Fig. 12). The gas is ejected from the small hole, while the solution covered the gas and maintained its original shape, which is difficult to keep the stable and continuous solution surface.

Fig. 16 (a) Schematic of bubble rupture of the airflow-assisted needle. (b) Jet morphology when pulsed air pressure is assisted. (c) Jet morphology when pulsed air pressure is ventilated. (c) Single-needle pulse pressure deposition. Fiber morphology. (e) Statistical distribution of fiber diameter. (f) Microscopic SEM image of fiber (12 wt%, $t_1 = 100$ ms, $t_2 = 2000$ ms)



Under the same gas pressure, the larger diameter of inner gas pipe produced greater pressure on the liquid film. Therefore, the larger bubbles can be generated.

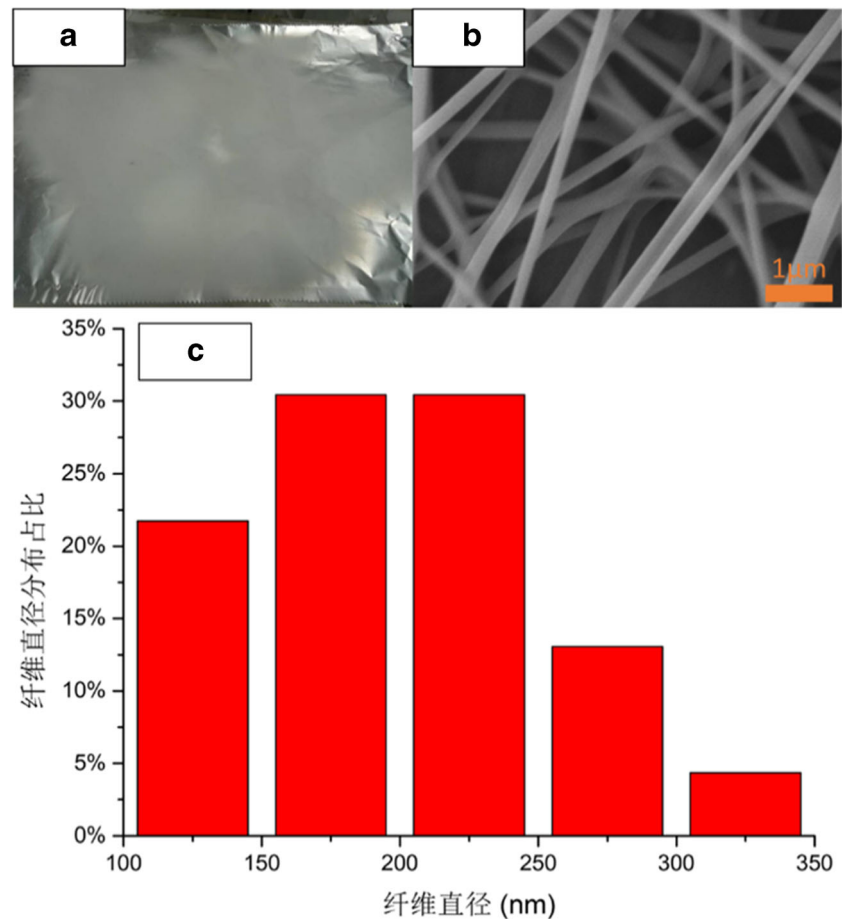
Figure 13 a–c show the fiber deposition on the collector using 8G–13G, 8G–16G, and 8G–20G, respectively. When spinning with 8G–13G and 8G–16G needles, they could produce large disturbance on the surface of the solution, and the thickness of fiber deposition was large. However, as shown in Fig. 13b, the spinning with 8G–16G needle was unstable, and more small bubbles were generated on the collector (shown by the yellow circle), mainly because the fragment liquid film generated by the needle was quite thick. When the fragment liquid film deposited on the collector, it did not fully stretch into nanofibers in the electric field, which in turn affected the quality of the fiber membrane. The spinning using 8G–20G needle is shown in Fig. 13c. As the volume of gas from the airhole was small, the gas disturbance on the surface of the solution was relatively small and the gas impulse to the liquid film was weak. There were no fragment liquid film flies to the air and hardly any small bubbles on the collector. But the spinning efficiency was relatively low as the effect of gas assisting was not good. However, due to the small diameter of 8G–20G

needle, the clogging phenomenon was easy to occur, which made it difficult to spin continuously for a long time.

4.3 Effect of solution concentration on spinning process

In the gas-assisted electrospinning process, solution concentration and solubility have strong influence on its viscosity and viscous bubble, thereby affecting the formation of bubble liquid film in the electric field. In this experiment, the PVA solution was adopted to investigate the effect of concentration on spinning, and the results were shown in Fig. 14 a–d. Figure 14a shows the jet deposition morphology at 8 wt.% PVA. The viscosity of the solution was small, and the bubbles were easily detached from the needle. Though the pulse gas was applied, the bubbles often directly break away from the needle and hit the collector before rupture. Therefore, a large liquid film appeared on the collector. When using a 10 wt.% PVA solution, as shown in Fig. 14b, due to the small viscous force, the gas flow tended to make liquid film with continuous bubbles at a certain pressure. And at the moment of ventilation, many bubbles directly flied to the collector. Therefore, a lot of solution was not fully stretched, resulting in poor quality nanofibers. Figure 14c

Fig. 17 Spinning fiber morphology of the four-needle array; (b) SEM image of fiber; (c) statistical chart of fiber diameter distribution



shows when the concentration was 12 wt%, the spinning process was more stable, and bubbles rarely presented on the collector. This was because when the viscosity of the solution reached a certain level, the gas pressure can make the liquid film rupture during ventilation. The liquid film had a good fluidity to cover the gas pipe mouth quickly. The gas pressure during the gas-closing period was not enough to make the liquid film rupture again, so the formation and fracture of the bubbles could be well controlled. After the liquid film ruptured, the gas force was insufficient, so only a small amount of liquid film was torn to form fragments and flied to the collector. With the well-controlled spinning voltage and distance, good results have been obtained. With 14 wt.% PVA, the spinning efficiency was low. Although no small droplets appeared on the collector, the viscosity of the solution was large, which deteriorate the fluidity of the liquid film as show in Fig. 14d. When the top of a bubble breaks, the solution cannot cover the pore, which makes the generation of bubbles unstable, resulting in unsustainable spinning.

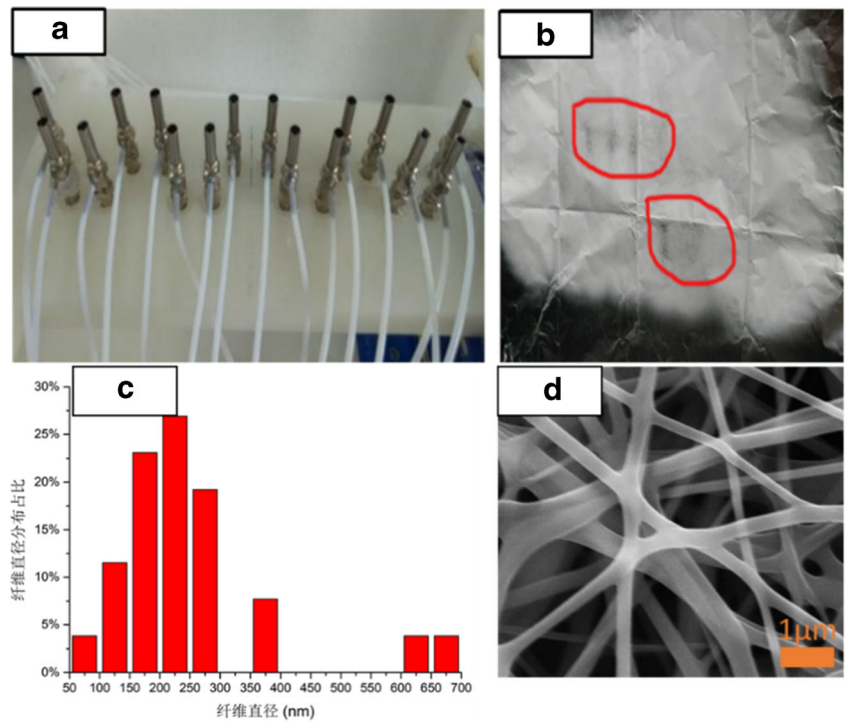
4.4 Production improvement by gas-assisted needle

For the ordinary 8G single needle at 45 kV, because the needle was large, the charge density of the liquid surface was

insufficient. In the absence of gas disturbance, it was difficult to spontaneously induce the jet. It was necessary to use the needle tip to move the liquid surface at the beginning to give a disturbance to the surface of the solution, and this could start the spinning. Moreover, the number of jet streams generated during the spinning process was only 1–2, as shown in Fig. 15a. Since there was no disturbance on the solution, it was not possible to splash droplet, and the film on the collector was relatively flat (Fig. 15b) with 0.06 g for half an hour spinning. The fiber diameter distribution diagram was shown in Fig. 15d, and most of the fiber diameters were distributed between 150 and 250 nm.

Figure 16a is a schematic diagram of the instantaneous rupture of the liquid film. When using the pulse gas flow, the liquid film breaks, the edge of the liquid film would produce many small protrusions, likely to induce jets in the electric field. If the electric field energy is sufficient, a plurality of jets could be induced. Figure 16 b–c show that there were 2–4 jet strands during the gas-off period and 5–6 jets were generated at the moment of ventilation, indicating that under the disturbance of the gas, more jets could be generated at a lower voltage energy. As the disturbance level at the needle was relatively high under the pulse gas, the spinning distance and voltage did not adjusted to the optimal parameters, so there

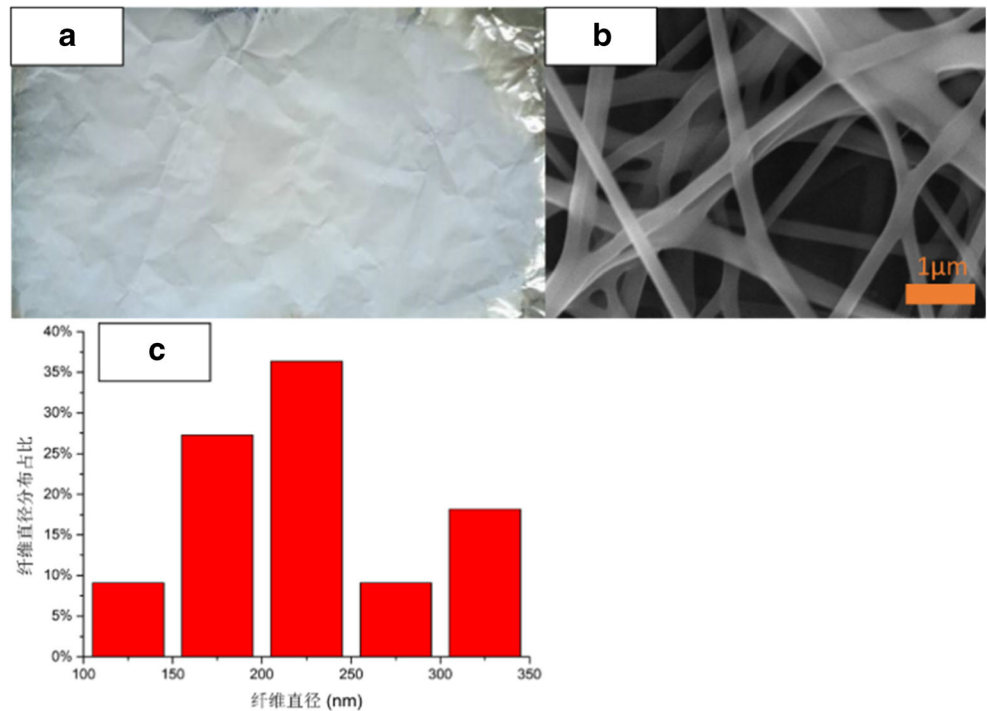
Fig. 18 (a) Picture of the needle; (b) gas-free auxiliary 8G array 16-pin electrospinning half-hour deposition fiber morphology; (c) statistical analysis of fiber diameter; (d) SEM image of sample



were droplets on the spun film, as shown in Fig. 16d. The half-hour spinning mass was 0.17 g, which was nearly three times that of ordinary 8G needles. Figure 16e was a fiber diameter chart of the SEM image, and it can be seen that more than 70% of the fiber deposition diameters were between 150 and 250 nm.

To improve the gas-assisted electrospinning yield, we increase the number of needles by using trapezoidal array four-needle needle. The pressure was 0.1 MPa, $t_1 = 100$ ms, $t_2 = 800$ ms, liquid supply was 4 ml/h, spinning voltage was 45 kV, spinning distance was 20 cm, and good spinning effect was obtained. Figure 17 shows the aluminum foil after spinning

Fig. 19 (a) Half-hour deposition effect of 16-needle airflow assisted needle fiber; (b) SEM image of the sample; (c) statistical analysis of fiber diameter



deposition, exhibiting the good morphology without any small droplet. This was mainly because the pressure and gas flow were smaller and the gas bubbles were stable after the air pressure was dispersed by the four needles. Using these parameters for spinning, the mass of half-hour deposited nanofiber was 0.483 g, which was about three times than that of a single-needle electrospinning can produce. The interaction between the needles in the array has played the role. The charge density of the single needle was low, and the energy obtained by each needle jet was small. Compared to the single needle, although the spinning efficiency of each needle was reduced, the stable batch spinning has been achieved by increasing the voltage. It can be seen from Fig. 17c that 80% or more of the fiber diameter distribution was between 100 and 250 nm.

Figure 18a shows the spinning device with 16 needles. The fibers deposited without pulse gas after half an hour is shown in Fig. 18b. Because the needle was stationary, and the jets directly repelled each other, it can be found that in the red circles the deposited fibers are uneven. Without being aerated for half an hour, the mass of deposited fiber was 0.27 g. Figure 18c showed a statistical analysis of the sample fibers. It can be seen that the distribution of fiber diameters was relatively large, and most of them were centered between 150 and 300 nm.

Figure 19 showed the fibers produced using gas flow assistance relative to Fig. 18. The gas pressure was 0.1 MPa, $t_1 = 100$ ms, $t_2 = 600$ ms, liquid rate was 14 mL/h, spinning voltage 45 kV, and distance 20 cm. With these parameters, we had achieved good result, no dripping and uniform fiber deposition. After half-hour continuous spinning, the process was still stable, and the half-hour produced 1.26 g fiber (7.4 times of gas-assisted single-needle) which was 4.7 times of the air-free electrospinning needle. Further increasing the voltage can improve the fiber output. As can be seen from Fig. 19c, the fibers were all distributed between 100 and 350 nm, with 60% of the fiber diameters being between 150 and 250 nm.

5 Conclusions

Multi-needle electrospinning was further optimized to improve the production efficiency of nanofibers of per unit needle. The authors designed a coaxial pulse gas-assisted electrospinning device, which uses gas to regularly disturb the bubble, causing the bubble break at the tip to maintain multiple jets. The experimental results show that (1) constant gas-assistance is not easy to obtain a stable jet; (2) pulse gas pressure can better control the formation and rupture of bubble; (3) low-concentration solution has low viscosity, and air bubbles can easily separate the solution from gas pipe port and fly to collector; (4) if tracheal port is too small, gas pressure is insufficient to break the liquid film; and (5) the efficiency of 16-pin gas-assisted electrospinning needle is 4.7 times higher

than that of the air-free spinning process. This research provides a new idea for the high-efficient production of nanofibers.

Funding information This work was financially supported by Science and Technology Project of Guangdong Province (2017B090911012), University Innovation and Entrepreneurship Education Major Project of Guangzhou City (Item Number: 201709P05), Project of Science and Technology of Foshan City(2015IT100152), Key Laboratory Construction Projects in Guangdong (2017B030314178), Project of Jihua Laboratory (No.X190071UZ190), and Science and Technology Program of Guangzhou, China (No.201803010065).

Compliance with ethical standards

Conflict of interest The authors declare that they have no conflict of interest.

References

- Poellmann MJ, Johnson AJW (2014) Multimaterial polyacrylamide: fabrication with electrohydrodynamic jet printing, applications, and modeling. *Biofabrication* 6(3):12. <https://doi.org/10.1088/1758-5082/6/3/035018>
- Luzio A, Canesi EV, Bertarelli C, Caironi M (2014) Electrospun polymer fibers for electronic applications. *Materials* 7(2):906–947. <https://doi.org/10.3390/ma7020906>
- Wendorff JH, Agarwal S, Greiner A (2012) *Electrospinning: materials, processing, and applications*, vol 1. Wiley-VCH, Hoboken
- Garg K, Bowlin GL (2011) Electrospinning jets and nanofibrous structures. *Biomicrofluidics* 5(1). <https://doi.org/10.1063/1.3567097>
- Jiang G, Zhang S, Qin X (2016) Effect of processing parameters on free surface electrospinning from a stepped pyramid stage. *J Ind Text* 45(4):483–494. <https://doi.org/10.1177/1528083714537101>
- Shin HU, Li Y, Paynter A, Nartetamrongsutt K, Chase GG (2015) Vertical rod method for electrospinning polymer fibers. *Polymer* 65:26–33. <https://doi.org/10.1016/j.polymer.2015.03.052>
- Holopainen J, Penttinen T, Santala E, Ritala M (2015) Needleless electrospinning with twisted wire spinneret. *Nanotechnology* 26(2):025301
- Salehuddin HS, Mohamad EN, Wan NLM, Afifi AM (2017) Multiple-jet electrospinning methods for nanofiber processing: a review. *Mater Manuf Process* 33:479–498. <https://doi.org/10.1080/10426914.2017.1388523>
- Zhang CC, Gao CC, Chang MW, Ahmad Z, Li JS (2016) Continuous micron-scaled rope engineering using a rotating multi-nozzle electrospinning emitter. *Appl Phys Lett* 109(15):151903
- Xu J, Liu C, Hsu PC, Liu K, Zhang R, Liu Y, Cui Y (2016) Roll-to-roll transfer of electrospun Nanofiber film for high-efficiency transparent air filter. *Nano Lett* 16(2):1270
- Wang H, Li M, Chen X, Zheng J, Chen X, Zhu Z (2015) Study of deposition characteristics of multi-nozzle near-field electrospinning in electric field crossover interference conditions. *AIP Adv* 5(4). <https://doi.org/10.1063/1.4902173>
- Reneker DH, Yarin AL (2008) Electrospinning jets and polymer nanofibers. *Polymer* 49(10):2387–2425. <https://doi.org/10.1016/j.polymer.2008.02.002>
- YAMASHITA Y, Ko F, TANAKA A, MIYAKE H (2007) Characteristics of elastomeric nanofiber membranes produced by electrospinning. *J Text Eng* 53(4):137–142

14. Vaseashta A (2007) Controlled formation of multiple Taylor cones in electrospinning process. *Appl Phys Lett* 90(9):093115
15. Paruchuri S, Brenner MP (2007) Splitting of a liquid jet. *Phys Rev Lett* 98(13):134502
16. Wang X, Lin T, Wang X (2015) Use of airflow to improve the nanofibrous structure and quality of nanofibers from needleless electrospinning. *J Ind Text* 45(2):310–320. <https://doi.org/10.1177/1528083714537100>
17. Liu Y, He J-H (2007) Bubble electrospinning for mass production of nanofibers. *Int J Nonlin Sci Numer Simul* 8(3):393–396
18. Huang X, Wu D, Zhu Y, Sun D, Ieee (2007) Needleless Electrospinning of Multiple Nanofibers. 2007 7th Ieee conference on nanotechnology, Vol 1–3
19. Bird JC, de Ruiter R, Laurent C, Stone HA (2010) Daughter bubble cascades produced by folding of ruptured thin films. *Nature* 465(7299):759–762
20. Byakova AV, Gnyloskurenko SV, Nakamura T, Raychenko OI (2003) Influence of wetting conditions on bubble formation at orifice in an inviscid liquid : mechanism of bubble evolution. *Colloids Surf A Physicochem Eng Asp* 218(1):73–87
21. Chen R, Wan Y, Si N, He J-H, Ko F, Wang S-Q (2015) Bubble rupture in bubble electrospinning. *Therm Sci* 19(4):1141–1149
22. Chen RX (2015) On surface tension of a bubble under presence of electrostatic force. *Therm Sci* 19(1):353–355. <https://doi.org/10.2298/tsci141214149c>
23. He J-H (2008) Nano bubble dynamics in spider spinning system. *J Anim Vet Adv* 7(2):207–209
24. He J-H (2012) Effect on temperature on surface tension of a bubble and hierarchical ruptured bubbles for nanofiber fabrication. *Therm Sci* 16(1):327–330
25. He J-X, Qi K, Zhou Y-M, Cui S-Z (2014) Fabrication of continuous nanofiber yarn using novel multi-nozzle bubble electrospinning. *Polym Int* 63(7):1288–1294. <https://doi.org/10.1002/pi.4672>
26. Jian Z, Yong Y, Chen Q, Yu Z (2017) Experimental study and numerical simulation of periodic bubble formation at submerged micron-sized nozzles with constant gas flow rate. *Chem Eng Sci* 168:1–10
27. Li Z-B, Liu H-Y, Dou H (2014) On air blowing direction in the blown bubble-spinning. *Materia-Brazil* 19(4):345–349
28. Liu F-J, Dou H (2013) A modified Yang-Laplace equation for the bubble electrospinning considering the effect of humidity. *Therm Sci* 17(2):629–630
29. Nahra HK, Kamotani Y (2000) Bubble formation from wall orifice in liquid cross-flow under low gravity. *Chem Eng Sci* 55(20):4653–4665
30. Vafaei S, Angeli P, Wen D (2011) Bubble growth rate from stainless steel substrate and needle nozzles. *Colloids Surf A Physicochem Eng Asp* 384(1):240–247
31. Vafaei S, Wen D (2010) Bubble formation on a submerged micronozzle. *J Colloid Interface Sci* 343(1):291–297
32. Yuewen D (2016) Experimental study on the formation and movement of bubbles in water. Xinjiang University
33. Nieminen HJ, Laidmäe I, Salmi A, Rauhala T, Paulin T, Heinämäki J, Hæggeström E (2018) Ultrasound-enhanced electrospinning. *Sci Rep-Uk* 8(1):4437
34. Delnoij E, Kuipers JAM, Swaaij WPMV (1997) Dynamic simulation of gas-liquid two-phase flow: effect of column aspect ratio on the flow structure. *Chem Eng Sci* 52(21–22):3759–3772
35. Russell TP, Lin Z, Schäffer E, Steiner U (2003) Aspects of electrohydrodynamic instabilities at polymer interfaces. *Fibers Polym* 4(1):1–7
36. Schäffer E, ThurnAlbrecht T, Russell TP, Steiner U (2001) Electrohydrodynamic instabilities in polymer films. *Epl* 53(4): 518–524
37. Xie S (2003) Quantitative discussion on the static induction law of spherical conductors in a uniform electric field. *J Binzhou Univ* 19(2):45–47
38. Qu C, Yu Y, Zhang J (2017) Experimental study of bubbling regimes on submerged micro-orifices. *Int J Heat Mass Transf* 111:17–28
39. Yuanping H (2015) Study on the mechanism of charged droplet breakage and electrohydrodynamic characteristics. Jiangsu University

Publisher's note Springer Nature remains neutral with regard to jurisdictional claims in published maps and institutional affiliations.